Viscoplastic fingering in rectangular channels

A. Eslami* and S. M. Taghavi*
Department of Chemical Engineering, Université Laval, Québec, Québec Canada G1V 0A6

(Received 11 March 2020; revised 22 June 2020; accepted 20 July 2020; published 10 August 2020)

We experimentally study the viscous fingering problem of viscoplastic fluids in channels of rectangular cross section. We find that a yield stress-dependent capillary number (Ca^*) and an aspect ratio-dependent Bond number (Bo^*) can classify the finger shape into *ramified* and *unified* fingering patterns, and the finger flow regime into *yield stress*, *viscosity*, and *aspect ratio-buoyancy*-dominated regimes. For these regimes, we provide the transition boundaries using Ca^* and Bo^* and propose simple relations to predict the finger width, for a wide range of flow parameters, versus the capillary number, the channel aspect ratio, and the rheology of the viscoplastic fluid.

DOI: 10.1103/PhysRevE.102.023105

I. INTRODUCTION

As the precursor to diverse pattern formations, interfacial instabilities appear, to give a few examples, in fractal growth, crystal growth, thermal plumes, electroosmotic flows, etc [1,2]. Among interfacial flows of wide interest, the classical Saffman-Taylor instability [3] or viscous fingering occurs when air displaces a viscous liquid in a Hele-Shaw channel. Aside from the beauty and complexity of viscous fingering flow patterns, these interfacial flows are of importance as they appear in a variety of natural phenomena and industrial applications, with prominent examples in oil and gas industries, food processing, and biomedical and biotechnological applications [4]. In fact, most natural and industrial materials, including paints, pastes, glues, inks, blood, slurries, muds, fresh concrete, etc., are complex fluids [5,6], particularly exhibiting viscoplastic behavior [7,8]. For imposed stresses below a critical value called the yield stress ($\hat{\tau}_y$) [9], viscoplastic materials respond like elastic solids; when the yield stress is overcome, the viscoplastic materials flow like truly viscous fluids [5]. In stark contrast to their Newtonian fluid counterparts, our understanding of viscous fingering of viscoplastic fluids is not mature, despite the prevalence and diversity of viscous fingering phenomena of viscoplastic fluids.

For Newtonian fluids in a Hele-Shaw channel, as air moves within the viscous liquid, it forms a unified (single) finger that advances at a constant velocity and the finger width ($\hat{w}$) is determined by the capillary number, $Ca = \hat{\mu}\hat{U}/\hat{\sigma}$, i.e., the ratio of viscous and capillary forces, where $\hat{\mu}$ is the liquid viscosity, $\hat{U}$ is the finger-tip velocity, and $\hat{\sigma}$ is the surface tension coefficient. The variation in the channel aspect ratio, $\delta = \hat{W}/\hat{b}$, with $\hat{b}$ and $\hat{W}$ being the gap thickness and the channel width, does not modify the fingering pattern, i.e., for high [3], moderate [10,11], and low [12–14] aspect ratios, there is always a unified finger within the channel. It must be also noted that, when varying the aspect ratio through increasing the gap thickness, buoyancy becomes non-negligible, the effects of which are assessed in a number of studies, using the Bond number, i.e., the ratio of buoyant to surface tension forces, defined as $Bo = \hat{\rho}\hat{g}\hat{b}^2/\hat{\sigma}$, where $\hat{\rho}$ is the liquid density and $\hat{g}$ is the gravitational acceleration [11,12,15].

Compared to Newtonian fluids, the fingering patterns for viscoplastic fluids are quite different [16–22]. In particular, for these fluids at lower velocities of air, a ramified (branched) fingering pattern is formed, for which $\hat{w}$ is independent of $\hat{U}$ (i.e., the yield stress-dominated regime). At lager imposed velocities of air, a unified fingering pattern appears, for which $\hat{w}$ continuously decreases with $\hat{U}$ (i.e., the viscosity-dominated regime). For these fluids, the formation of the ramified fingering pattern is attributed to the dominance of the yield stress and the existence of unyielded zones in regions behind the finger front [23–25]. Despite these useful findings, a complete picture of the viscous fingering problem for viscoplastic fluids is still unavailable as their dynamics is highly nonlinear in nature. In particular, the effects of the channel aspect ratios and buoyancy, in combination with the yield stress, surface tension, and viscosity, on viscous fingering of viscoplastic fluids are unknown. In other words, although some of the general features of the aforementioned regimes have been described in the literature, the previous works have been limited to the channels of large aspect ratios ($\delta \gtrsim 27$), where the effect of buoyancy is negligible ($Bo \lesssim 0.3$) [24–26]. Therefore, it is insightful to investigate the influence of Bo and δ together with the other governing dimensionless flow parameters on the flow regimes.

In this paper, we present experimental results on the formation of different fingering patterns emerging from the injection of air into a Hele-Shaw channel of different rectangular cross sections, filled with a viscoplastic fluid. We systematically investigate the effects of the channel width ($\hat{W}$), the gap thickness ($\hat{b}$), the imposed or finger-tip velocity ($\hat{V}$ or $\hat{U}$), and the yield stress ($\hat{\tau}_y$) on the viscous fingering features of viscoplastic fluids. The experiments cover a wide range of aspect ratios ($1 \leqslant \delta \leqslant 200$) and buoyancy forces ($0.002 \leqslant Bo \leqslant 4.45$). We uncover that the aspect ratio and buoyancy, in combination with the yield stress, viscosity, and surface tension, exert remarkable impacts on the flow, inhibiting or

*Corresponding authors: Ali.Eslami.1@ulaval.ca; Seyed-Mohammad.Taghavi@gch.ulaval.ca

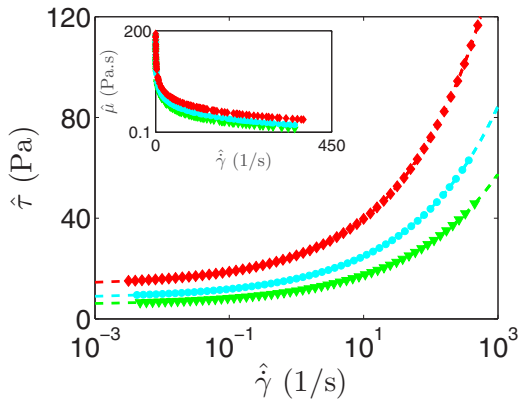

FIG. 1. Flow curves of the shear stress, $\hat{\tau}$, vs the shear rate, $\hat{\dot{\gamma}}$, from steady shear tests. The lines correspond to the Herschel-Bulkley model parameters fitted to the data. The data correspond to three different Carbopol concentrations, called for simplicity as high (♦), medium (●), and low (▼) Carbopol concentrations. The inset shows the variation of the effective viscosity vs the shear rate for the same data as in the main figure.

triggering the formation of ramified and unified fingering patterns. Analyzing the role of the flow characteristic stresses, we succeed in providing a reasonable picture of the flow, via classifying the flow regimes and proposing predictions to the finger width in different regimes, versus appropriate dimensionless groups that elegantly combine the aspect ratio, surface tension, viscosity, yield stress, and buoyancy.

II. EXPERIMENTS

In our experiments, air displaces a Carbopol gel, i.e., a common viscoplastic fluid, at different Carbopol concentrations, in channels of different rectangular cross sections. The rheological properties of the Carbopol gel are quantified using a rheometer (DHR-3 TA Instrument) via a parallel-plate geometry (gap 1 mm, diameter 40 mm). Fine sandpapers are attached to the rheometer plates to eliminate wall slip. The shear behavior of the Carbopol gel can be described by the Herschel-Bulkley model [27,28]:

$$\hat{\tau} = \hat{\tau}_y + \hat{\kappa}\hat{\dot{\gamma}}^n.$$

This is a well-known constitutive equation for viscoplastic fluids, which includes the shear stress ($\hat{\tau}$), the shear rate ($\hat{\dot{\gamma}}$), the consistency index ($\hat{\kappa}$), and the power-law index (n). Using the Herschel-Bulkley model, the effective viscosity can be written as

$$\hat{\mu} = \hat{\tau}_y(\hat{\dot{\gamma}})^{-1} + \hat{\kappa}(\hat{\dot{\gamma}})^{n-1},$$

which depends on both the Carbopol concentration and the shear rate.

The flow curves measured using rotational tests are shown in Fig. 1. In steady conditions, the graph shows the shear stress ($\hat{\tau}$) as a function of the shear rate ($\hat{\dot{\gamma}}$), for the three Carbopol concentrations. As seen, at low shear rates, these Carbopol gels clearly exhibit a yield stress and increasing the Carbopol concentration results in enhancing the yield stress value. The dashed lines superimposed on Fig. 1 demonstrate that the three Carbopol gel samples are well fitted using the Herschel-Bulkley model, for which the rheology can be described by

$$\text{low Carbopol concentration:} \quad \hat{\tau} = 5.4 + 5.7\,\hat{\dot{\gamma}}^{0.32};$$
$$\text{medium Carbopol concentration:} \quad \hat{\tau} = 8.3 + 7.6\,\hat{\dot{\gamma}}^{0.31};$$
$$\text{high Carbopol concentration:} \quad \hat{\tau} = 13.7 + 11.6\,\hat{\dot{\gamma}}^{0.35}.$$

These samples exhibit strong yield stress and shear-thinning behavior ($n < 0.4$), implying a remarkable deviation from Newtonian viscosity behavior (see the inset of Fig. 1).

In terms of dimensional parameters, the experiments are designed to investigate the effects of the channel width ($\hat{W}$), the gap thickness ($\hat{b}$), and the imposed velocity ($\hat{V}$), at different Carbopol concentrations, on the viscous fingering features of viscoplastic fluids. A large number of channels with different rectangular cross sections are made out of acrylic plastic plates, each of length $\hat{L} = 50$ cm, for which the gap thickness ($0.1 \leqslant \hat{b} \leqslant 5.5$ mm) and the channel width ($3 \leqslant \hat{W} \leqslant 130$ mm) are varied. See the middle image in Fig. 2 for a schematic view of the experimental setup. The channel is initially filled with a Carbopol gel sample, dyed with black ink for visualization. Then, through an inlet, air is injected into the channel. The air imposed velocity is controlled via a mass flow controller and the interface evolution is recorded with a high-speed camera (Basler acA2040), from the channel top view. Postprocessing is carried out using MATLAB. For the preparation of this study, more than 2000 experiments are performed.

It is known that viscoplastic fluids can slip on smooth solid surfaces, for example, the acrylic plastic plates that make our Hele-Shaw channels. The wall slip effects in Carbopol gel flows, especially at lower shear rates, may result in a deviation of the effective rheological parameters from the ones measured in the rheometry (in which sandpapers are typically used to avoid slippage); however, the previous works have shown that these effects may be of importance only when the gap thickness is smaller than 0.4 mm [29], which is not the case in most of our experiments (where $\hat{b}$ in most of our channels is larger than 0.5 mm). In addition, a comparison between the rheological measurements of the Carbopol gels using smooth plates compared against rough plates (using sandpapers) reveals that the slippage starts to affect the rheological measurements only at smaller shear rates, typically $\hat{\dot{\gamma}} < 0.1$, which orderwise is comparable with the values reported in the literature [30]. Using the average value of the gap thickness and the lowest velocities in our experiments results in a characteristic shear rate that is always greater than 0.1, implying that our experiments are not affected by the wall slip. Finally, our recent work with a similar range of rheological parameters reveals the presence of thin static wetting films of the Carpool gels attached to the upper and lower plates of the Hele-Shaw channels, after the passage of the displacing finger, confirming that there is no slippage in our experiments [25].

III. RESULTS AND DISCUSSION

Figure 2 shows two main flow patterns as a function of $\hat{b}$, $\hat{W}$, and $\hat{V}$; the Carbopol concentration is constant. Depending on the flow parameters, a unified or ramified fingering pattern

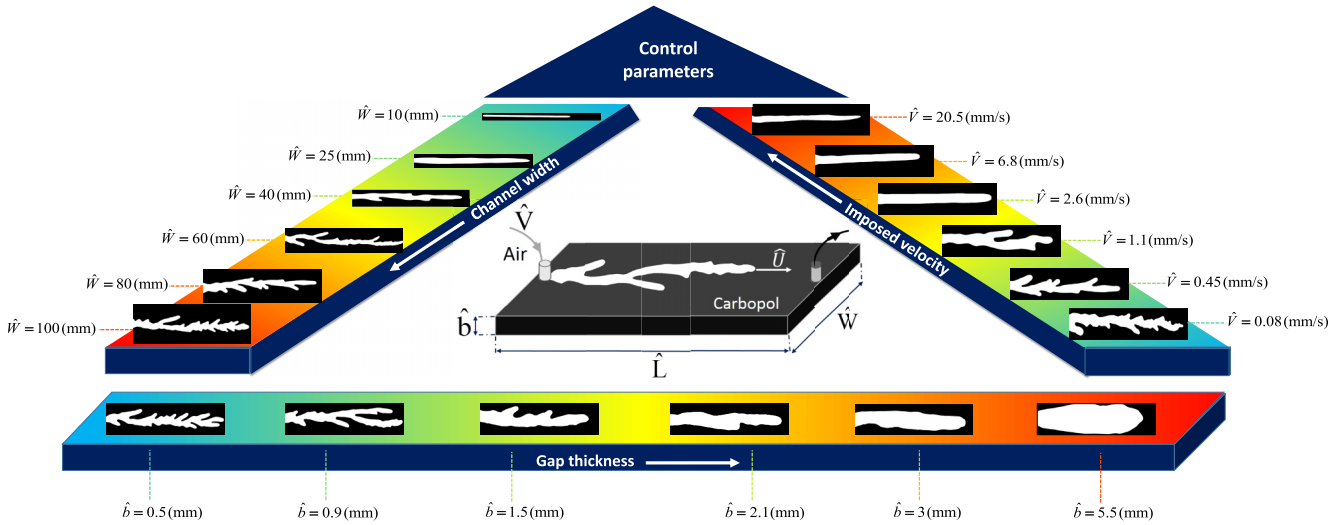

FIG. 2. Diagram of two flow patterns, i.e., unified and ramified fingering patterns, as a function of the dimensional control parameters in this study, including the channel width ($\hat{W}$), the gap thickness ($\hat{b}$), and the air imposed velocity ($\hat{V}$). The middle image shows the schematic of the 3D experimental setup and the other images are the 2D top view experimental images. The results for the low Carbopol concentration are shown, while similar results are observed for moderate and high Carbopol concentrations. The air finger flows from left to right in all images.

is observed. For small $\hat{V}$ (or equivalently small $\hat{U}$), the yield point is not exceeded everywhere in the viscoplastic fluid, leading to the domination of the yield stress; consequently, the initial finger frequently splits without feeling the surroundings and forms several asymmetric fingers, leading to the formation of the ramified fingering pattern. By increasing the velocity, the yield stress is overcome and the flow becomes dominated by the viscosity; the finger shape transitions from a ramified to a unified fingering pattern. The unified finger moves in the channel center and it is relatively thin; these are characteristics of a viscous finger. When $\hat{b}$ increases, resulting in increasing buoyancy, a similar behavior is observed: The flow transitions from the yield stress-dominated regime to one in which buoyancy dominates the flow, while the finger shape transitions from a ramified to a unified fingering pattern. The unified finger is quite wide [11], i.e., the characteristic of a buoyant finger. An opposite effect to that of $\hat{b}$ and $\hat{V}$ is seen for $\hat{W}$: At small values of $\hat{W}$ (i.e., small aspect ratios) there is a unified finger, which at large values of $\hat{W}$ (i.e., large aspect ratios) becomes destabilized and develops into a ramified finger. The flow transitions from a regime where the low aspect ratio is critical to one where the aspect ratio is not important and the yield stress dominates. These results emphasize that the flow parameters such as the aspect ratio, yield stress, surface tension, viscosity, and buoyancy have significant effects on the fingering pattern as well as the finger width.

Let us attempt to find the appropriate dimensionless groups that can explain the key flow features observed so far. First of all, our results show that the ramified fingering pattern appears at lower imposed velocities, where the yield stress is predominant. At higher velocities, on the other hand, there is a unified finger mainly controlled by a balance between the surface tension stress ($\hat{\sigma}/\hat{b}$) and the viscous stress ($\hat{\mu}\hat{U}/\hat{b}$), as the yield stress is no longer dominant. In order to consider all these effects mentioned, i.e., the yield, viscous, and surface tension stresses, into a single dimensionless group, let us define a yield stress-dependent capillary number, Ca*:

$$\mathrm{Ca}^* = \frac{\overbrace{\left(\frac{\hat{\mu}\hat{U}}{\hat{b}}\right)}^{\text{viscous stress}} \times \overbrace{\left(\frac{\hat{\mu}\hat{U}}{\hat{b}}\right)}^{\text{viscous stress}}}{\underbrace{\hat{\tau}_y}_{\text{yield stress}} \times \underbrace{\left(\frac{\hat{\sigma}}{\hat{b}}\right)}_{\text{surface tension stress}}} = \frac{(\hat{\mu}\hat{U})^2}{\hat{\tau}_y \hat{b}\hat{\sigma}}, \tag{1}$$

in which the numerator represents the viscous stress and the denominator includes the yield and surface tension stresses. Equation (1) can be also presented in the form of

$$\mathrm{Ca}^* = \frac{\left(\frac{\hat{\mu}\hat{U}}{\hat{\sigma}}\right)^2}{\left(\frac{\hat{\tau}_y\hat{b}}{\hat{\sigma}}\right)} = \frac{\mathrm{Ca}^2}{\overline{\mathrm{Ca}}}, \tag{2}$$

where Ca is the traditional capillary number and $\overline{\mathrm{Ca}}$ is a *viscoplasto-capillary* number obtained by replacing the effective viscosity ($\hat{\mu}$) in the traditional capillary number by the yield viscosity [$\hat{\tau}_y(\hat{b}/\hat{U})$], leading to $\overline{\mathrm{Ca}} = \hat{\tau}_y\hat{b}/\hat{\sigma}$. Note that one can also write

$$\mathrm{Ca}^* \equiv \frac{\mathrm{Ca}}{\mathrm{Bn}},$$

where the Bingham number ($\mathrm{Bn} = \frac{\hat{\tau}_y}{\hat{\mu}\frac{\hat{U}}{\hat{b}}}$) represents a dimensionless yield stress number, which is zero for Newtonian fluids [31]. Moreover, our results show that the ramified fingering pattern occurs when the values of $\hat{W}$ and $\hat{b}$ are large and small, respectively. The effects of the former can be considered via the cross-section aspect ratio, δ, while the effects of the latter are typically evaluated via the Bond number, Bo, which in combination with δ results in an aspect ratio-dependent Bond number (Bo*):

$$\mathrm{Bo}^* = \frac{\mathrm{Bo}}{\delta} = \frac{\hat{\rho}\hat{g}\hat{b}^3}{\hat{\sigma}\hat{W}}. \tag{3}$$

The relation above is also equivalent to the ratio of the Archimedes number ($\mathrm{Ar} = \hat{\rho}^2\hat{g}\hat{b}^3/\hat{\mu}^2$) and the Laplace

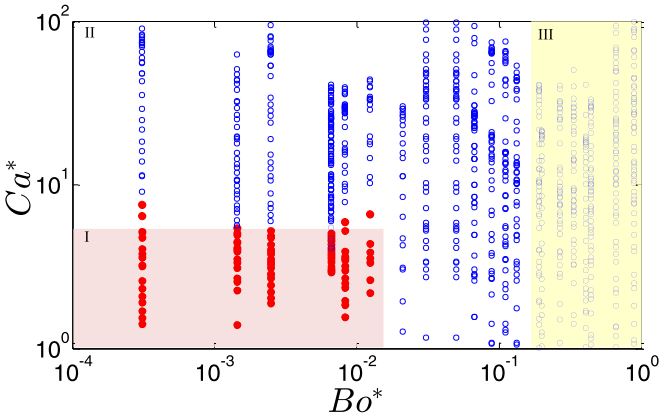

FIG. 3. Fingering pattern classification in the plane of Bo^* and Ca^*, for the ramified (filled symbols) and unified (hollow symbols) fingering patterns. Three finger flow regimes associated with Fig. 4, i.e., the yield stress, viscosity, and aspect ratio-buoyancy-dominated regimes, are also marked by I, II, and III as well as red, white, and yellow colored areas. The critical transition boundaries between the colored areas are at $Ca^* \approx 5$, $Bo^* \approx 0.015$, and $Bo^* \approx 0.2$.

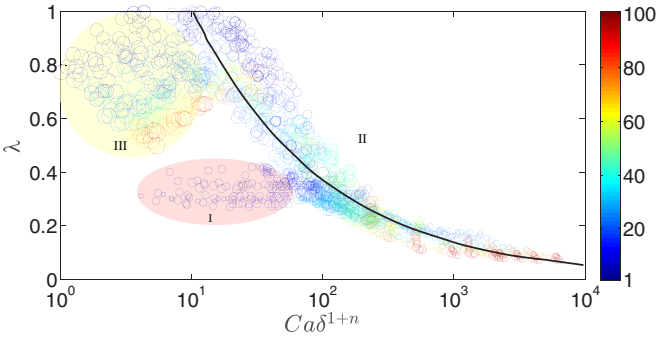

FIG. 4. Relative finger width, λ, vs $Ca\delta^{1+n}$ for ≈2000 experimental data at different conditions. The values of Ca^* and Bo^* are illustrated by the color and size of the circles, respectively; the values of $Ca^* \in [1\ 10^2]$ are given in the color bar; the values of $Bo^* \in [10^{-4}\ 1]$ are represented by the circle size: Larger circles represent larger values of Bo^*. Three different flow regimes associated to the colored areas in Fig. 3, i.e., the yield stress, viscosity, and aspect ratio-buoyancy-dominated regimes, are marked by I, II, and III, respectively.

number ($La = \hat{\rho}\hat{\sigma}\hat{W}/\hat{\mu}^2$):

$$Bo^* = \frac{Bo}{\delta} \equiv \frac{Ar}{La}. \tag{4}$$

For a wide range of flow parameters (i.e., $1 \leqslant Ca^* \leqslant 10^2$ and $10^{-4} < Bo^* \leqslant 1$), Fig. 3 classifies the experimental data in the plane of Ca^* and Bo^*, where the unified and ramified fingering patterns are reasonably segregated using the hollow and filled symbols, with the critical boundaries at $Ca^* \approx 5$ and $Bo^* \approx 0.015$. At small values of Bo^* or Ca^*, the appearance of the ramified fingering pattern is due to the dominance of the yield stress over the other forces; however, at higher Bo^* (Ca^*), the buoyant (viscous) stress competes with the yield stress to balance the surface tension, resulting in the unified fingering pattern. When $Bo^* > 0.015$, the unified fingering pattern is observed, independent of the value of Ca^*. Similarly, when $Ca^* > 5$ the unified fingering pattern is seen, independent of the value of Bo^*.

In addition to the fingering pattern, a key parameter in the viscous fingering problem is the relative finger width ($\lambda = \hat{w}/\hat{W}$), the variation of which versus a proper scaling parameter is of interest. For Newtonian fluids, this scaling parameter is $Ca\delta^2$ [32,33] (which can be theoretically rationalized based on the maximum growth wavelength obtained using the linear stability analysis). When the experimental results of the relative finger width are plotted versus $Ca\delta^2$, a universal master curve can be obtained for Newtonian fluids. For weakly shear-thinning fluids, the same rescaling is also valid if the viscosity is substituted by the shear dependent viscosity [34]. More recently, for large aspect ratios and in the absence of buoyancy, it has been shown that $Ca\delta^{1+n}$ is a relevant scaling parameter for viscoplastic fluids [25]. This scaling parameter agrees both with the Newtonian limit ($n = 1$), for which $Ca\delta^2$ is relevant, and the strongly shear-thinning viscoplastic limit ($n \ll 1$), for which $Ca\delta$ [24] has also provided satisfactory results. Figure 4 shows the variation of λ versus $Ca\delta^{1+n}$, for a wide spectrum of experimental parameters, for both unified and ramified fingering patterns. The values of Ca^* and Bo^* are represented by the color and size of the circles, respectively. On this figure, different finger flow regimes are marked by I, II, and III, the transition boundaries of which are presented in Fig. 3. For regime II, as the finger width continuously decreases with $Ca\delta^{1+n}$, all the experimental data reasonably fall onto a master curve found as

$$\lambda_{II} \approx \alpha_{II}\,(Ca\delta^{1+n})^{\beta_{II}}, \tag{5}$$

where the subscript denotes the finger flow regime here and elsewhere, and $\alpha_{II} = 2.85$ and $\beta_{II} = -0.44$ are the best-fit parameters in our work. Regime II is dominated by viscosity, and it coincides with the unified fingering pattern, with $Ca^* > 5$ or $Bo^* > 0.015$ limited to $Bo^* < 0.02$ (see Fig. 3).

Looking into the literature, it is worth noting that the exponent value in the equation above (β_{II}) seems to depend on the fluid types and it varies in the previous experimental results, finding, for example, for Newtonian fluids $\beta_{II} \in [(-0.15) - (-0.11)]$ [3,33,35,36], for shear-thinning fluids $\beta_{II} \in [(-0.22) - (-0.18)]$ [34,37], and for viscoplastic fluids $\beta_{II} \in [(-0.67) - (-0.48)]$ [24,26]. The first thing to notice is that the exponent value is not constant in the previous works even for simple fluids (i.e., Newtonian fluids). The reason may be attributed to the control parameter in which the displaced film thickness left behind the fingers is neglected [33]. The second thing to notice is that, on average, the absolute value of β_{II} for viscoplastic fluids is nearly four times larger than that for Newtonian ones, implying that the finger width in viscoplastic fluids decreases versus the control parameter at a much higher rate compared to that for Newtonian fluids.

Unlike regime II in Fig. 4, the data for regimes I and III do not fall on the master curve. In fact, for regime I, which is dominated by the yield stress and corresponds to the ramified fingering pattern, λ is nearly independent of $Ca\delta^{1+n}$. As the yield stress is the critical parameter of the flow in this regime, the finger width is expected to be a function of the viscoplasto-capillary number, $\overline{Ca}$, which indeed turns out to be the case:

Using our experimental data, we are able to find that

$$\lambda_{\mathrm{I}} \approx \alpha_{\mathrm{I}}(\delta^2\overline{\mathrm{Ca}})^{\beta_{\mathrm{I}}}, \tag{6}$$

valid for $\mathrm{Ca}^* \leqslant 5$ and $\mathrm{Bo}^* \leqslant 0.015$ (see Fig. 3). In this equation, we find $\alpha_{\mathrm{I}} = 5.5$ and $\beta_{\mathrm{I}} = -0.5$. While the exponent $\beta_{\mathrm{I}} = -0.5$ can be supported by theory [23–25], the coefficient $\alpha_{\mathrm{I}} \approx 5.5$ in Eq. (6) is a constant found in our experiments. The form of Eq. (6) is in agreement with the previous findings from various studies, only with different fitting coefficients: $\alpha_{\mathrm{I}} \approx 8.1$ [26], $\alpha_{\mathrm{I}} \approx 4.2$ [24], and $\alpha_{\mathrm{I}} \approx 3.2$ [38]. These differences between the values of α_{I} may be generally due to various experimental conditions, uncertainties, and also differences in the surface tension coefficient value; in fact, the existence of a yield stress makes the surface tension measurement for viscoplastic fluids very difficult [39,40].

Finally for regime III, which occurs when the aspect ratio-dependent Bond number is very large, there is a unified finger and the finger width is significantly affected by buoyancy or the aspect ratio. Thus, in this regime the experimental data do not collapse onto the master; instead, the finger width remains large (i.e., $\lambda \gtrsim 0.5$) and it is a complex function of the yield stress, buoyancy, viscosity, and aspect ratio. For this regime, we crudely find

$$\lambda_{\mathrm{III}} \approx 0.75 \pm 0.25. \tag{7}$$

which is valid for $\mathrm{Bo}^* \gtrsim 0.2$ (see Fig. 3).

It may be insightful to remember that, while the yield stress-dependent capillary number (Ca^*) is used to separate regimes I and II, the traditional capillary number (Ca) and the viscoplasto-capillary number ($\overline{\mathrm{Ca}}$) with various powers of the aspect ratio are relevant for scaling the relative finger width in these regimes. In other words, the data points of regimes I and II are clearly segregated using the appropriate combination of $\overline{\mathrm{Ca}}$ and Ca, leading to Ca^* (see Fig. 3), whereas Ca^* itself is not appropriate to describe the finger-width variations; this is simply because of the domination of different forces in different regimes. For example, in regime I, the finger width is determined by a balance between the surface tension stress and the yield stress, independent of $\hat{U}$. In this case, $\overline{\mathrm{Ca}}$, which is independent of the velocity, becomes naturally relevant, as Ca^* includes the velocity term and is therefore inappropriate. In regime II, on the other hand, the finger width is determined by a balance between the viscous stress (narrowing the finger) and the surface tension stress (widening the finger); therefore, Ca is relevant, while $\mathrm{Ca}^* \equiv \mathrm{Ca/Bn}$ would be expectedly unable to describe the finger-width variation, simply due to the presence of the extra Bn in the denominator.

Regime III

The aspect ratio-buoyancy-dominated regime (i.e., regime III) in our experiments is associated with an efficient removal of the viscoplastic displaced fluid and the presence of a wide, unified finger in the Hele-Shaw channel. Since this regime has not been reported before in the context of viscous fingering of viscoplastic flows, it is useful to describe its flow features, mainly based on analyzing the finger-width variation versus the flow parameters. In dimensional form, the main experimental flow parameters are the gap thickness ($\hat{b}$), the yield stress ($\hat{\tau}_y$), the channel width ($\hat{W}$), and the finger-tip velocity ($\hat{U}$), the effects of which on the relative finger width (λ) will be qualitatively described in this section. For comparison purposes only, the variation of λ in regimes I and II will be also presented alongside that in regime III; however, as the focus of this section is on regime III, the interested reader is referred to Refs. [20,24,25] for a detailed analysis and understanding of the effect of the flow parameters on λ in regimes I and II.

Figure 5 plots the variation of λ versus $\hat{U}$ for different values of $\hat{b}$ in regime III, in comparison with that in regimes I and II. As seen, λ increases with $\hat{b}$, regardless of the flow regime. One justification for the observed behavior in regime III may be that increasing $\hat{b}$ improves the transverse buoyancy force within the channel gap, which has some consequences. First of all, it affects the pressure drop across the finger tip [11], which in return affects the finger-tip shape and curvatures. Second, and perhaps more important, it lifts the displacing finger from the channel bottom wall and pushes it toward the channel top wall; consequently, the residual layers of the displaced fluid become thinner and thicker on the channel top and bottom walls, respectively [11,41]. Loosely speaking, as the residual layers of the displaced fluid on the lower wall becomes progressively thicker in the transverse direction, the finger must become wider in the lateral direction (simply due to mass conservation), which leads to an increase in λ.

The effects of increasing $\hat{\tau}_y$ on the variation of λ versus $\hat{\tau}_y$ is plotted in Fig. 6. As seen, there is a significant difference between the effect of the yield stress on the relative finger width in regime III, compared to that in regimes I and II. In the viscosity- and yield stress-dominated regimes, increasing the yield stress results in decreasing the finger width as shown in Figs. 6(b) and 6(c) (also see Refs. [24,25] for physical explanations). However, in the aspect ratio-buoyancy-dominated regime, the finger width increases with the yield stress, within the ranges explored [see Fig. 6(a)]. This further highlights the flow complexity in this regime.

A possible justification for the observed effects of $\hat{\tau}_y$ on λ in regime III may be related to the residual wall layers of the displaced fluid. These layers, for which the thickness is a function of several flow parameters such as the yield stress value, can notably affect the flow features. In regime III, as the flow geometry approaches a 3D one due to the small aspect ratio (and the large gap thickness), the displacing finger feels the presence of all four channel walls, implying that the effect of the residual wall layers on the flow become even more significant. There are numerous studies in the viscoplastic displacement flow context [42–47], revealing that by increasing the yield stress the wall residual layer thickness decreases. In fact, increasing the yield stress affects the plug ahead of the finger, which reduces the residual layer thickness [48–50]. Regarding regime III, in which the aspect ratio is small, it may be argued that the most notable decrease in the residual layer thickness (as the yield stress increases) can be in the lateral direction, resulting in increasing λ [see Fig. 6(a)]. Loosely speaking, by increasing the yield stress, the resistance ahead of the finger front increases, causing the finger to expand most remarkable in the lateral direction and become widened.

To analyze the effect of the channel width in regime III compared with that in regimes I and II, Fig. 7 shows the

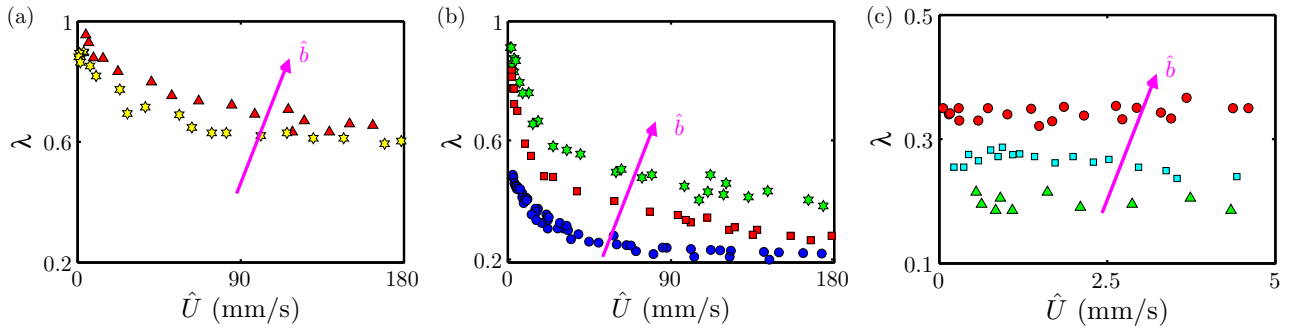

FIG. 5. Variation of λ vs $\hat{U}$ in (a) regime III, (b) regime II, and (c) regime I, at fixed parameter sets. The gap thickness increases in the solid arrow direction. The flow parameters in each subfigure are as follows. (a) At fixed channel width ($\hat{W} = 15$ mm) and Carbopol concentration (low) with $\hat{b} = 4.3$ mm (▲); $\hat{b} = 3$ mm (★). (b) At fixed channel width ($\hat{W} = 40$ mm) and Carbopol concentration (medium) with $\hat{b} = 3$ mm (★); $\hat{b} = 2.1$ mm (■); $\hat{b} = 1.5$ mm (●). (c) At fixed channel width ($\hat{W} = 68$ mm) and Carbopol concentration (low) with $\hat{b} = 1.5$ mm (●); $\hat{b} = 1$ mm (■); $\hat{b} = 0.5$ mm (▲).

variation of λ versus $\hat{U}$, for given parameter sets. First of all, λ decreases with $\hat{U}$ in regimes III and II but is independent of $\hat{U}$ in regime I. However, increasing $\hat{W}$ increases λ in regime III, decreases λ in regime II, and has no significant effect on λ in regime I. It is interesting that $\hat{W}$ has an opposite effect on λ in regimes III and II. It seems that, independent of the finger velocity, the finger-width selection mechanism in the aspect ratio-buoyancy-dominated regime is completely different from that in the viscosity-dominated regime. In fact, the presence of three-dimensional effects in regime III, compared to primarily two-dimensional effects in regimes I and II, makes the understanding of the underlying physics behind the finger width variation more difficult. Examples of these three-dimensional effects include a modified pressure drop across the finger front, the presence and importance of the residual layers of the Carbopol gel on the four walls, the finger front three-dimensional dynamics, etc.

One critical question is whether regime III is governed by the balance between buoyancy and surface tension, buoyancy and yield stress, or the combination of these forces. To answer to this question, let us first provide an estimation of the surface tension effect compared to the yield stress effect, quantified via the viscoplasto-capillary number varying in the range of $0.3 \lesssim \overline{\mathrm{Ca}} \lesssim 1.2$ in regime III. This implies that, compared to the yield stress, the effect of the surface tension in regime III is less pronounced than that in regimes I and II, for which $\overline{\mathrm{Ca}}$ can be as small as 0.008. However, since $\overline{\mathrm{Ca}}$ is still an order 1 parameter, the effect of the surface tension cannot be totally ignored in regime III. On the other hand, for the yield number [6,51,52], which can be written as

$$Y = \frac{\hat{\tau}_y}{\hat{\rho}\hat{g}\hat{b}} \equiv \frac{\overline{\mathrm{Ca}}}{\mathrm{Bo}},$$

we find that $0.1 \lesssim Y \lesssim 0.4$ in regime III, suggesting the importance of buoyancy in this regime. Note that the yield number value can be much larger in regimes I and II (e.g., up to 13). Considering that the dimensionless parameters present intermediate values in regime III, i.e., $0.3 \lesssim \overline{\mathrm{Ca}} \lesssim 1.2$ and $0.1 \lesssim Y \lesssim 0.4$, we can crudely say that the force balance is among the yield stress, buoyancy, and surface tension forces in this regime.

Regime III in our work has certain similarities with the Newtonian viscous fingering flows at larger values of the aspect ratio-dependent Bond numbers (Bo^*), where the traditional scaling law for λ breaks down and the collapse of the λ data onto a single curve is not possible. Based on the Newtonian literature, the Saffman-Taylor-like system breaks down when $\mathrm{Bo}^* \gtrsim 0.16$ (which is calculated based on the results of Ref. [10]). This value is slightly smaller than that

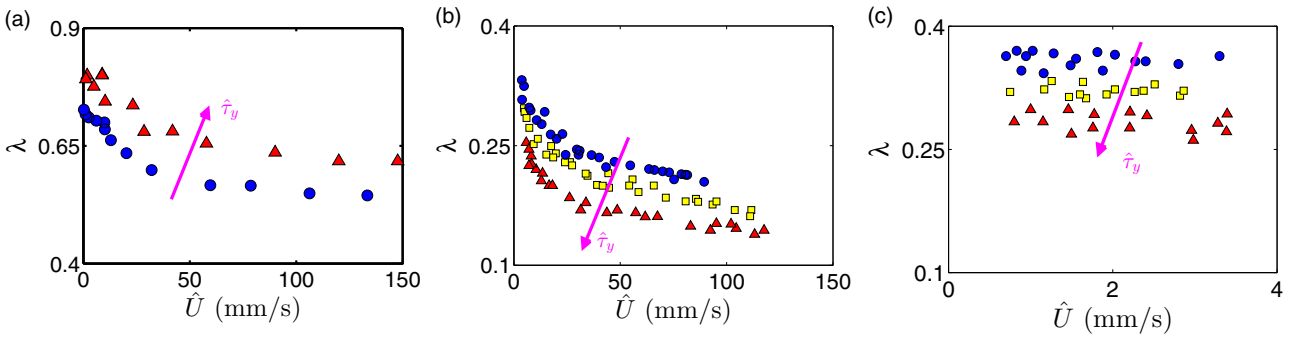

FIG. 6. Variation of λ vs $\hat{U}$ in (a) regime III, (b) regime II, and (c) regime I, at fixed parameter sets. The yield stress increases in the solid arrow direction. The data correspond to three different Carbopol concentrations: low (●), medium (■), and high (▲) Carbopol concentrations. The other flow parameters are (a) $\hat{b} = 3$ mm and $\hat{W} = 6$ mm; (b) $\hat{b} = 1.5$ mm and $\hat{W} = 60$ mm; and (c) $\hat{b} = 1.5$ mm and $\hat{W} = 45$ mm.

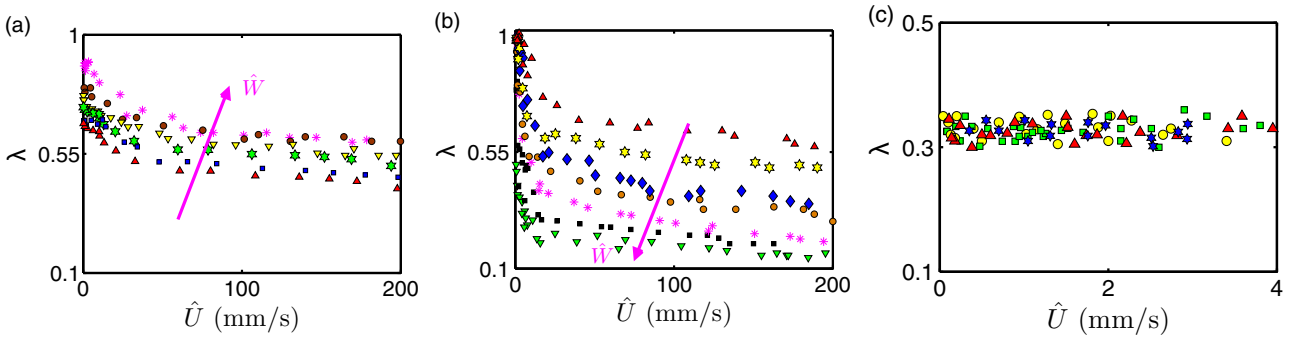

FIG. 7. Variation of λ vs $\hat{U}$ in (a) regime III, (b) regime II, and (c) regime I, at fixed parameter sets. The channel width increases in the solid arrow direction. The flow parameters in each subfigure are as follows. (a) At fixed gap thickness ($\hat{b} = 3$ mm) and Carbopol concentration (low) with $\hat{W} = 15$ mm (⋆); $\hat{W} = 12$ mm (●); $\hat{W} = 9$ mm (▼); $\hat{W} = 6$ mm (★); $\hat{W} = 4.5$ mm (■); $\hat{W} = 3$ mm (▲). (b) At fixed gap thickness ($\hat{b} = 3$ mm) and Carbopol concentration (low) with $\hat{W} = 130$ mm (▼); $\hat{W} = 80$ mm (■); $\hat{W} = 60$ mm (⋆); $\hat{W} = 45$ mm (●); $\hat{W} = 36$ mm (◆); $\hat{W} = 30$ mm (★); $\hat{W} = 21$ mm (▲). (c) At fixed gap thickness ($\hat{b} = 1.5$ mm) and Carbopol concentration (medium) with $\hat{W} = 100$ mm (■); $\hat{W} = 80$ mm (★); $\hat{W} = 60$ mm (●); $\hat{W} = 40$ mm (▲).

found in our work, e.g., $\mathrm{Bo}^* \approx 0.2$, suggesting a difference between Newtonian and viscoplastic fingering flows when buoyancy becomes significant.

In the context of regime III, there are other differences between Newtonian and viscoplastic fingering flows. For example, Fig. 8 compares the variation of λ versus $\mathrm{Ca}\delta^{1+n}$ for viscoplastic fluids (filled symbols) against their corresponding Newtonian fluids (hollow symbols [10]) with comparable parameters. As seen, λ decreases with increasing $\mathrm{Ca}\delta^{1+n}$ and increases with increasing δ, for both Newtonian and viscoplastic cases. As also seen, the values of λ in the Newtonian fluids are generally larger than those in the viscoplastic fluids. In addition, while the aspect ratio seems to only slightly affect the finger width in the Newtonian cases, its effects are much more pronounced in the viscoplastic cases (e.g., see the distance between the curves in the viscoplastic cases). Finally, the finger-width data for Newtonian fluids remain close to one other for different values of δ and they seem to progressively approach a master curve at large values of δ, which is not the case for viscoplastic fluids.

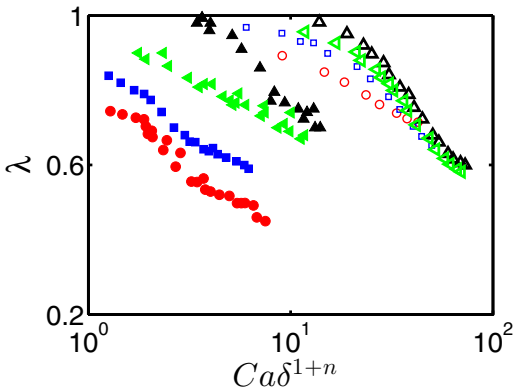

FIG. 8. Variation of λ vs $\mathrm{Ca}\delta^{1+n}$ in viscoplastic fluids of the current work (filled symbols) and Newtonian fluids from the literature (hollow symbols), for fixed values of $\hat{b}$ and $\hat{W}$. For Newtonian fluids ($n = 1$), the control parameter, i.e., $\mathrm{Ca}\delta^{1+n}$, reverts back to $\mathrm{Ca}\delta^2$. The data corresponding to four different aspect ratios are $\delta = 1$ (●, ○) $\delta = 2$ (■, □), $\delta = 4$ (◂, ◁), $\delta = 5$ (▲, △). All the data are for $\mathrm{Bo}^* > 0.2$, i.e., regime III.

Let us end this section by remembering that our description of regime III in this section has been mainly qualitative; for instance, we have not attempted to propose a scaling law to superimpose the finger-width data on a single curve in this regime (we do not even claim that such a simple scaling law exists). In fact, as we have partly seen, the flow behaviors in the aspect ratio-buoyancy-dominated regime is complex due to the presence of a variety of flow parameters and features. Considering this, a computational analysis of the flow, providing an in-depth insight into the flow details within the channel gap thickness, seems to be appropriate as a future research direction, to bring to light the flow physics behind regime III.

IV. CONCLUSION

In conclusion, we demonstrated that the viscous fingering instability of viscoplastic fluids can be significantly affected by the channel cross-section aspect ratio and buoyancy, in combination with the surface tension, viscosity, and yield stress. We found that the finger destabilization due to the yield stress, resulting in the ramified fingering pattern, can be damped at higher values of a yield stress-dependent capillary number (Ca^*) and an aspect ratio-dependent Bond number (Bo^*), leading to the unified fingering pattern. Based on the finger-width variation, we classified the flow regimes into yield stress (I), viscosity (II), and aspect ratio-buoyancy-dominated (III) regimes, for which we proposed simple relations to predict the finger width versus appropriate scaling parameters that included the capillary number, the channel aspect ratio, and the rheology of the viscoplastic fluid.

ACKNOWLEDGMENTS

This research has been carried out at Université Laval, supported financially via the Canada Foundation for Innovation (Grants No. GF112622, No. GQ113034, and No. GF517657) and the Discovery Grant of the Natural Sciences and Engineering Research Council of Canada (Grant No. CG10915).

We thank the reviewers for their invaluable comments. We wish to also acknowledge the help of Anirban Bhattacharjee, supported by a MITACS Globalink Research Internship, in conducting the experimental tests.

[1] M. Mirzadeh and M. Z. Bazant, Phys. Rev. Lett. **119**, 174501 (2017).
[2] T. Gao, P. Mirzadeh, M. Bai, K. Conforti, and M. Bazant, Nat. Commun. **10**, 1 (2019).
[3] P. G. Saffman and G. I. Taylor, Proc. Royal Soc. London **245**, 312 (1958).
[4] G. M. Homsy, Annu. Rev. Fluid Mech. **19**, 271 (1987).
[5] P. Coussot, J. Non-Newt. Fluid Mech. **211**, 31 (2014).
[6] I. A. Frigaard, Curr. Opin. Colloid Interface Sci. **43**, 80 (2019).
[7] N. J. Balmforth, I. A. Frigaard, and G. Ovarlez, Annu. Rev. Fluid Mech. **46**, 121 (2014).
[8] C. Liu, A. De Luca, A. Rosso, and L. Talon, Phys. Rev. Lett. **122**, 245502 (2019).
[9] In this paper, we adopt the convention of denoting dimensional quantities with the ˆ symbol.
[10] A. de Lozar, A. L. Hazel, and A. Juel, Phys. Rev. Lett. **99**, 234501 (2007).
[11] A. De Lozar, A. Juel, and A. L. Hazel, J. Fluid Mech. **614**, 173 (2008).
[12] M. Magnini, S. Khodaparast, O. K. Matar, H. A. Stone, and J. R. Thome, Phys. Rev. Fluids **4**, 023601 (2019).
[13] A. L. Hazel and M. Heil, J. Fluid Mech. **470**, 91 (2002).
[14] O. Atasi, S. Khodaparast, B. Scheid, and H. A. Stone, Phys. Rev. Fluids **2**, 094304 (2017).
[15] S. S. Mamba, F. Zoueshtiagh, and M. Baudoin, Int. J. Multiph. **113**, 343 (2019).
[16] O. Fadoul and P. Coussot, Fluids **4**, 53 (2019).
[17] J. V. Fontana, S. A. Lira, and J. A. Miranda, Phys. Rev. E **87**, 013016 (2013).
[18] A. Eslami, R. Basak, and S. M. Taghavi, Ind. Eng. Chem. Res. **59**, 4119 (2020).
[19] S. Ahmadikhamsi, F. Golfier, C. Oltean, E. Lefèvre, and S. Bahrani, Phys. Fluids **32**, 012103 (2020).
[20] A. Eslami and S. M. Taghavi, J. Non-Newt. Fluid Mech. **264**, 25 (2019).
[21] H. Caliman, E. Soares, and R. Thompson, J. Non-Newt. Fluid Mech. **247**, 207 (2017).
[22] J. V. Fontana and J. A. Miranda, Phys. Rev. E **88**, 023001 (2013).
[23] P. Coussot, J. Fluid Mech. **380**, 363 (1999).
[24] A. Lindner, P. Coussot, and D. Bonn, Phys. Rev. Lett. **85**, 314 (2000).
[25] A. Eslami and S. M. Taghavi, J. Non-Newt. Fluid Mech. **243**, 79 (2017).
[26] N. Maleki-Jirsaraei, A. Lindner, S. Rouhani, and D. Bonn, J. Phys.: Condens. Matter **17**, S1219 (2005).
[27] M. Maillard, J. Boujlel, and P. Coussot, Phys. Rev. Lett. **112**, 068304 (2014).
[28] M. Dinkgreve, M. Fazilati, M. Denn, and D. Bonn, J. Rheol. **62**, 773 (2018).
[29] B. Geraud, L. Bocquet, and C. Barentin, Eur. Phys. J. E. **36**, 30 (2013).
[30] V. Bertola, F. Bertrand, H. Tabuteau, D. Bonn, and P. Coussot, J. Rheol. **47**, 1211 (2003).
[31] R. Thompson and E. Soares, J. Non-Newt. Fluid Mech. **238**, 57 (2016).
[32] C. Chevalier, A. Lindner, M. Leroux, and E. Clément, J. Non-Newt. Fluid Mech. **158**, 63 (2009).
[33] P. Tabeling and A. Libchaber, Phys. Rev. A **33**, 794 (1986).
[34] A. Lindner, D. Bonn, and J. Meunier, Phys. Fluids **12**, 256 (2000).
[35] C. Chevalier, M. Amar, D. Bonn, and A. Lindner, J. Fluid Mech. **552**, 83 (2006).
[36] J. W. McLean and P. G. Saffman, J. Fluid Mech. **102**, 455 (1981).
[37] A. Lindner, D. Bonn, E. Poire, M. Amar, and J. Meunier, J. Fluid Mech. **469**, 237 (2002).
[38] B. Ebrahimi, P. Mostaghimi, H. Gholamian, and K. Sadeghy, J. Eng. Math. **97**, 161 (2016).
[39] J. Boujlel and P. Coussot, Soft Matter **9**, 5898 (2013).
[40] L. Jørgensen, M. Le Merrer, H. Delanoë-Ayari, and C. Barentin, Soft Matter **11**, 5111 (2015).
[41] M. H. Jensen, A. Libchaber, P. Pelcé, and G. Zocchi, Phys. Rev. A **35**, 2221 (1987).
[42] A. Poslinski, P. Oehler, and V. Stokes, Polym. Eng. Sci. **35**, 877 (1995).
[43] M. Allouche, I. Frigaard, and G. Sona, J. Fluid Mech. **424**, 243 (2000).
[44] Y. Dimakopoulos and J. Tsamopoulos, J. Non-Newt. Fluid Mech. **112**, 43 (2003).
[45] P. de Souza Mendes, E. Dutra, J. Siffert, and M. Naccache, J. Non-Newt. Fluid Mech. **145**, 30 (2007).
[46] S. Taghavi, K. Alba, M. Moyers-Gonzalez, and I. Frigaard, J. Non-Newt. Fluid Mech. **167**, 59 (2012).
[47] A. Amiri, A. Eslami, R. Mollaabbasi, F. Larachi, and S. M. Taghavi, J. Non-Newt. Fluid Mech. **268**, 81 (2019).
[48] A. Eslami, I. Frigaard, and S. Taghavi, J. Non-Newt. Fluid Mech. **249**, 79 (2017).
[49] K. Wielage-Burchard and I. Frigaard, J. Non-Newt. Fluid Mech. **166**, 245 (2011).
[50] A. Eslami, R. Mollaabbasi, A. Roustaei, and S. M. Taghavi, Can. J. Chem. Eng. **97**, 2804 (2019).
[51] E. Chaparian and O. Tammisola, J. Fluid Mech. **885**, A45 (2020).
[52] D. I. Wilson, in *Lectures on Visco-Plastic Fluid Mechanics* (Springer, Berlin, 2019), pp. 195–259.